

See discussions, stats, and author profiles for this publication at: <https://www.researchgate.net/publication/262265629>

# Tailoring Au–Ag–S Composite Microstructures in One–Pot for Both SERS Detection and Photocatalytic Degradation of Plasticizers DEHA and DEHP

ARTICLE in ACS APPLIED MATERIALS & INTERFACES · MAY 2014

Impact Factor: 6.72 · DOI: 10.1021/am501898u · Source: PubMed

---

CITATIONS

6

---

READS

61

2 AUTHORS, INCLUDING:



Qi Cao

Helmholtz-Zentrum Dresden-Rossendorf

12 PUBLICATIONS 35 CITATIONS

SEE PROFILE

# Tailoring Au–Ag–S Composite Microstructures in One-Pot for Both SERS Detection and Photocatalytic Degradation of Plasticizers DEHA and DEHP

Qi Cao<sup>†</sup> and Renchao Che<sup>\*,†,‡</sup>

<sup>†</sup> Laboratory of Advanced Materials, Fudan University, Shanghai 200438, People's Republic of China

<sup>‡</sup> Department of Materials Science, Fudan University, Shanghai 200433, People's Republic of China

## S Supporting Information

**ABSTRACT:** We report a facile single-step one-pot solvothermal process for tailoring the Au–Ag–S microstructures as bifunctional substrates for both surface-enhanced Raman scattering (SERS) detection and photocatalytic degradation of plasticizers diethylhexyl phthalate (DEHP) and diethylhexyl adipate (DEHA). Typically, two different microstructures, the Ag<sub>2</sub>S particles inlaid Au microflowers (Ag<sub>2</sub>S–Au MFs) and Au particles decorated AgAuS microsheets (Au–AgAuS MSs) were obtained. The Ag<sub>2</sub>S–Au MF substrates finally turned out to provide  $0.9 \times 10^{-9}$  and  $0.9 \times 10^{-7}$  M of the limits of detection (LODs) for DEHP and DEHA in orange juice. And on the other hand, the Au–AgAuS MSs achieved complete degradation of DEHP and DEHA ( $1 \times 10^{-5}$  M) after 20 and 25 min of UV light irradiation, respectively. It is believed that the facile preparation and appreciable SERS and catalytic activities of these Au–Ag–S microstructures would make much sense to develop novel multifunctional sensing and monitoring devices.

**KEYWORDS:** gold, Ag<sub>2</sub>S, AgAuS, SERS, photocatalytic degradation, plasmon-enhanced



## INTRODUCTION

The many occurrences of plasticizers related food safety incidents have captivated much of people's attention on plasticizer contamination which usually derives from food packages or containers and was reported potential adverse effects on the reproductive systems and sexual differentiation of mankind.<sup>1,2</sup> Till now, various analytical techniques, for instance, the high-performance liquid chromatography,<sup>3</sup> tandem mass spectroscopy,<sup>4</sup> and colorimetric analysis,<sup>5</sup> have been developed for detecting these food contaminants. However, most of the current techniques are under restrictions of inadequate limits of detection (LODs) and complicated sample pretreatment steps such as extraction and preconcentration.<sup>6</sup> Moreover, considering the possibility to achieve *in situ* degradation of organic contaminants just on the detection substrates, to make a combination between the detection techniques and photocatalysis technology is of particular significance.

Surface-enhanced Raman spectroscopy (SERS), as an extremely sensitive and selective technique, can not only overcome those restrictions mentioned above, but also provide trace detection of various explosives,<sup>7</sup> narcotics,<sup>8</sup> pesticides<sup>9</sup> and biomolecules<sup>10,11</sup> down to single-molecule level.<sup>12,13</sup> Very recently, preliminary works on developing novel noble metal–semiconductor heterostructures based substrates, for example, the Au–Si,<sup>14</sup> Au–TiO<sub>2</sub>,<sup>15,16,23,26</sup> Ag–TiO<sub>2</sub>,<sup>17,18,24</sup> Ag–BN,<sup>19</sup> and ZnO–RGO–Au<sup>25</sup> systems, have achieved integration of SERS and photocatalytic process, and thus obtained photocatalytic degradation-induced self-cleaning SERS platforms<sup>14–20</sup> or inversely, the on-chip microreactors<sup>21,22</sup> for *in situ* SERS

monitoring of plasmon-enhanced catalytic reactions.<sup>21–26</sup> It is well-known that semiconductors, due to their unique band structures, are quite appropriate photocatalyst materials, while as SERS substrates, the enhancement they provide is usually much lower than those observed on metallic substrates. It is because that in semiconductor nanoparticles, the surface plasmon resonance (SPR) from the conduction band lies typically in the infrared band, thus the enhancement of Raman signals is totally contributed by charge transfer resonance (CTR).<sup>27</sup> In contrast, it is not only the CTR induced by noncovalent tight interactions between specific functional groups of analytes and the metallic surfaces, but also the localized surface plasmon resonance (LSPR) derived from the metal conduction band have made contributions to the huge enhancement of Raman signals in metal–analyte systems.<sup>28</sup> Hence in this regard, these noble metal–semiconductor composites hold great promise to offer both sensitive SERS detection and rapid photocatalytic degradation of organic pollutants, and thus are highly demanded for environmental applications nowadays.

Nevertheless, although many pioneer works have been done on this topic, until now, mainly focused on the combination of noble metal nanoparticles with semiconductor materials which have been intensively investigated (e.g., TiO<sub>2</sub><sup>15–18</sup> and ZnO<sup>25</sup>), while the heterostructures based on

Received: March 28, 2014

Accepted: May 12, 2014

Published: May 12, 2014

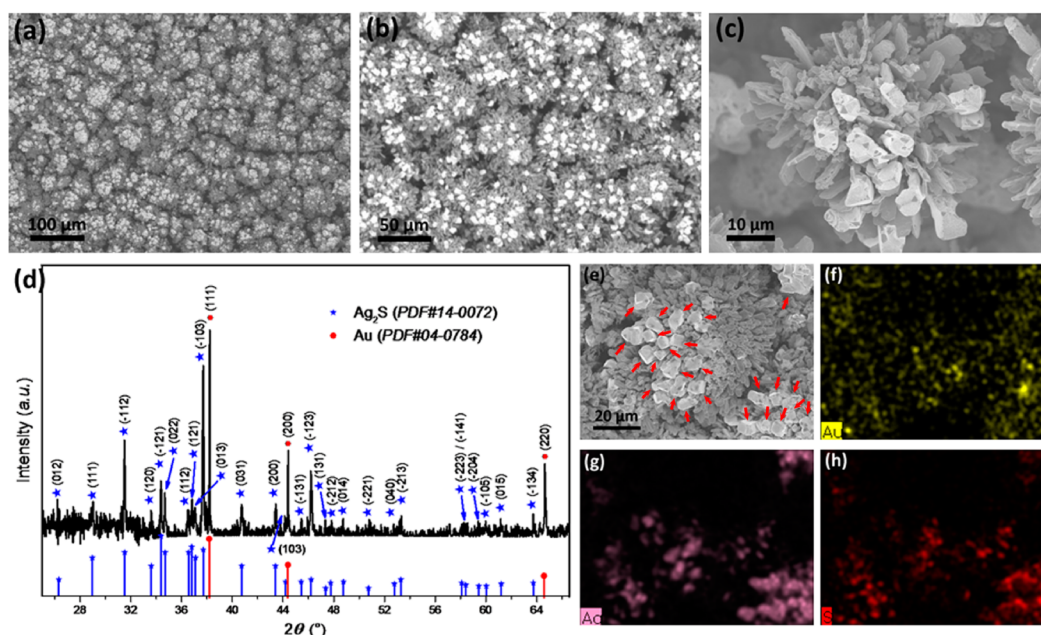


**Figure 1.** (a–c) SEM images obtained at different magnifications and (d) representative XRD pattern of the  $\text{Ag}_2\text{S}$ -Au MFs. (e–h) EDS element mapping of (f) Au, (g) Ag, and (h) S of the single MF shown in (e).

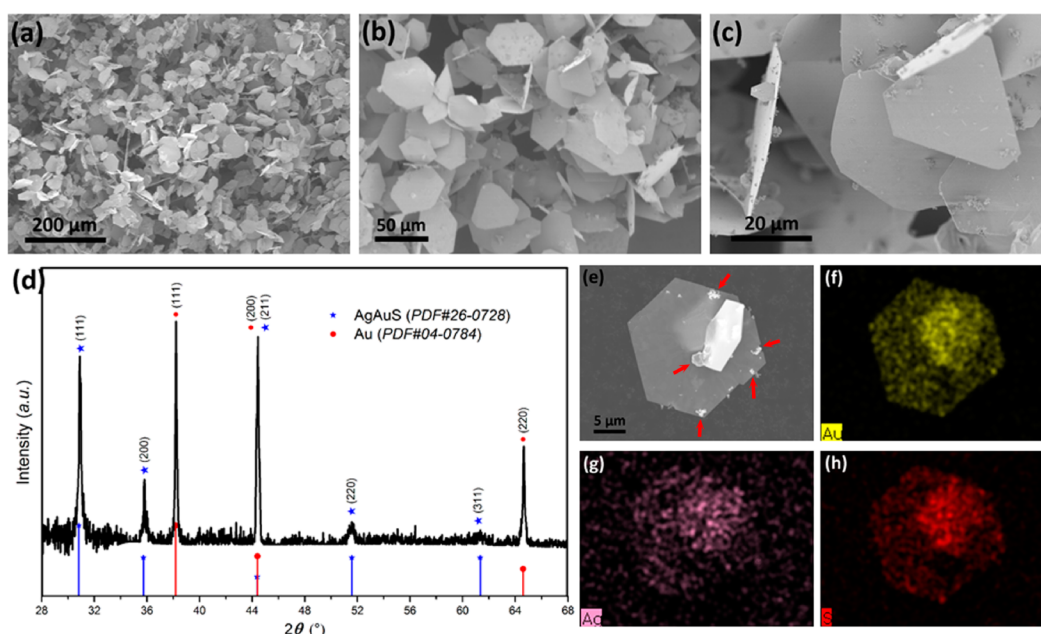


**Figure 2.** (a–c) SEM images obtained at different magnifications and (d) representative XRD pattern of the Au-AgAuS MSs. (e–h) EDS element mapping of (f) Au, (g) Ag, and (h) S of the two MSs shown in (e).

semiconducting noble metal sulfides were rarely studied. What's more, most of those intensively investigated semiconductors mentioned above possess wide band-gaps and thus have optical absorbance and emission in ultraviolet or visible band, whereas most of noble metal sulfides instinctively possess narrow band-gaps<sup>29</sup> and thus absorb in visible or near-infrared band. Because of this point, it is quite possible for them to capture a broader band of solar spectrum in practical applications. Besides, previous works have demonstrated the biocompatibility as well as low toxicity of these noble metal sulfides,<sup>30,31</sup> which is also a significant advantage for environmental and biomedical applications.

Here in this work, two different Au-Ag-S composite microstructures, specifically, the  $\text{Ag}_2\text{S}$  particle inlaid Au microflowers ( $\text{Ag}_2\text{S}$ -Au MFs) and Au particle decorated AgAuS microsheets (Au-AgAuS MSs) were obtained via a single-step one-pot solvothermal process. These Au-Ag-S microstructures were consequently applied as SERS and photocatalytic substrates for detection and degradation of the selected model molecules, the diethylhexyl phthalate (DEHP) and diethylhexyl adipate (DEHA) plasticizer. As a result, the  $\text{Ag}_2\text{S}$ -Au MF substrates demonstrated  $0.9 \times 10^{-9}$  and  $0.9 \times 10^{-7}$  M LODs for DEHP and DEHA, respectively, in orange juice. On the other hand, the Au-AgAuS MSs achieved complete degradation of DEHP and DEHA ( $1 \times 10^{-5}$  M) after

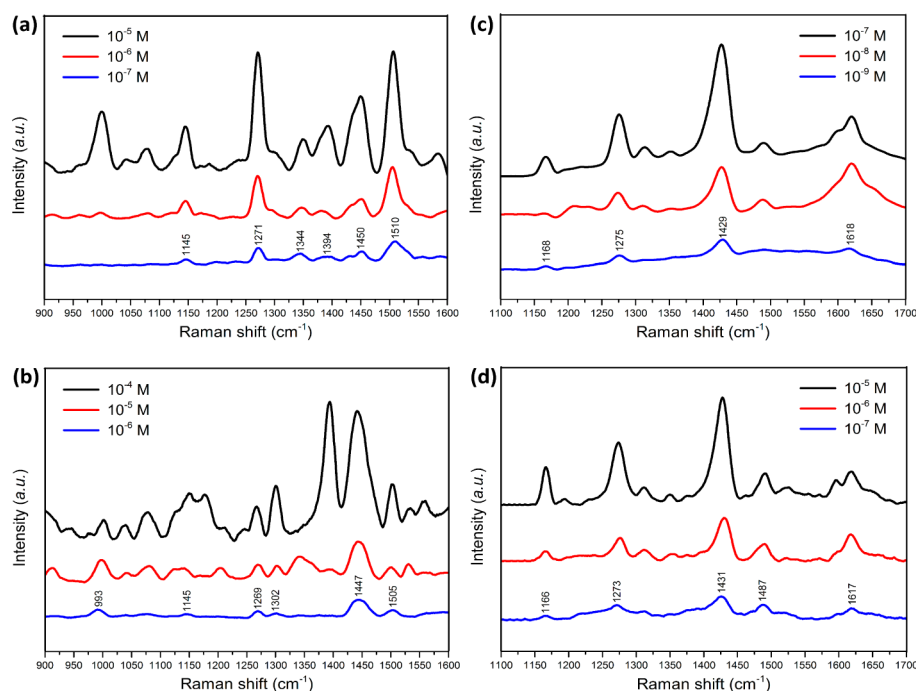


**Figure 3.** SERS spectra of the (a, b) DEHA and (c, d) DEHP ethanol solutions at different concentrations obtained on (a, c)  $\text{Ag}_2\text{S}$ -Au MF and (b, d) Au-AgAuS MS substrates, respectively.

20 and 25 min of UV light irradiation. It is to the best of our knowledge that although the micro/nanocomposites consisted of gold particles and narrow-band gap noble metal sulfides (typically,  $\text{Ag}_2\text{S}$ ,  $\text{Ag}_3\text{AuS}_2$ ,  $\text{AgAuS}$ ,  $\text{AuAgS}$ , and  $\text{Au}_2\text{S}$ ) have been synthesized and used for sensing applications,<sup>32–34</sup> the morphologies as well as application trails for SERS and photocatalytic bifunctional substrates described in this work are reported for the first time. In addition, the model molecules DEHP and DEHA were both very important and commonly used plasticizers nowadays. They have been involved in several serious food-safety scandals during the past few years. Nonetheless, works focused on their trace detection and rapid degradation are still lacking. Thus, in this regard, we consider this work to be more meaningful.

## RESULTS AND DISCUSSION

Figures 1 and 2 display the morphologies and phase constitutions of as-obtained  $\text{Ag}_2\text{S}$ -Au MFs and Au-AgAuS MSs. In the case of the MFs, SEM images in Figure 1a–c, e demonstrate the distinct flowerlike morphology. It seems that these flowerlike microstructures, with the sizes of dozens of micrometers, were derived from assemblies of pristine microplates and were additionally inlaid by another kind of small particles. The XRD pattern, as shown in Figure 1d, indicates that two components, the monoclinic  $\text{Ag}_2\text{S}$  (PDF#14–0072) and cubic Au (PDF#04–0784) were coexisted in these small particles inlaid MFs. EDS element mapping characterization was conducted to further identify the exact components of the particles and plates. As shown in Figure 1e–h, it can be inferred that the particles marked by red arrows should be  $\text{Ag}_2\text{S}$  since these areas possess relatively concentrated distributions of element Ag and S (Figure 1g, h), whereas in other areas occupied by assembled MFs, Au (Figure 1f) seems the dominant element. Hence, it can be roughly believed that these particle-inlaid MFs were actually  $\text{Ag}_2\text{S}$  particles inlaid Au MFs. On the other hand, in the case of the MSs, SEM images of

Figure 2a–c, e have revealed that these MSs were about several dozens of micrometers broad, whereas they were quite thin with the thicknesses much less than 1  $\mu\text{m}$ . Besides, it is observable that these MSs were decorated by another kind of small particles and chippings. Similarly through the correlated study with XRD and EDS mapping (Figure 2d–h), it can be deduced that the main phase of the obtained MSs was the ternary sulfide, cubic AgAuS (PDF#26–0728), whereas those scattered small particles, as are pointed out by red arrows in Figure 2e, were Au particles (PDF#04–0784). Thus, these MSs can be described as Au particles decorated AgAuS MSs. The EDS spectra of  $\text{Ag}_2\text{S}$ -Au MFs and Au-AgAuS MSs are shown in Figure S1 in the Supporting Information. Also, the Raman spectra of the MFs as well as MSs are given in Figure S2 in the Supporting Information as a supplement to the XRD results. Raman spectroscopy can provide valuable structural information on semiconductor materials. It is distinguishable in Figure S2 in the Supporting Information that resonance bands of the MSs locate near the wavenumbers of 242, 286, and 530  $\text{cm}^{-1}$ , whereas the bands of the MFs turn up at 286 and 530  $\text{cm}^{-1}$  only. It is according to previous reports that the resonant Raman scattering bands near 286 and 530  $\text{cm}^{-1}$  can be attributed respectively to the first- and second-order longitudinal optical phonon modes of the Ag–S bond in the lattice of  $\text{Ag}_2\text{S}$ ,<sup>35,36</sup> yet the band located at 242  $\text{cm}^{-1}$  should be assigned to the stretching mode of Au–S bond.<sup>37</sup> Therefore, it is rational that the MFs and MSs contain  $\text{Ag}_2\text{S}$  and AgAuS respectively since the Raman signals of Au–S bond were detected only in the MSs, whereas the Ag–S bond were detected in both samples. It is mentionable in addition that the observation of multiple Raman scattering bands indicates that the obtained  $\text{Ag}_2\text{S}$ -Au MFs and Au-AgAuS MSs possessed favorable optical qualities,<sup>35</sup> which should have positive effects on the photocatalytic degradation process.

To study the influence of the added amount of chloroauric acid on the eventual morphologies of the Au–Ag–S complexes,



0.4 or 1 mmol of chloroauric acid was added into methanol system and 20 mmol was added into the ethanol system instead, whereas the additions of Ag foil (1 piece) and sulfur powder (0.01 g) remained the same. As can be seen in Figure S3 in the Supporting Information, as the added amount of chloroauric acid was gradually increased in methanol, the  $\text{Ag}_2\text{S}$  maintained the shape of small particles with average sizes of 5–10  $\mu\text{m}$ , yet the Au product experienced distinct morphology transformation meanwhile from scattering clusters of Au particles with sizes smaller than 1  $\mu\text{m}$  (the 0.4 mmol case) to the larger-area distributed irregularly aggregated clusters of Au particles (the 1 mmol case), and finally to the orderly assembled flowerlike structures in which the basic units were elongated microplates with the average sizes in radial and longitudinal dimensions of about 5 and 25  $\mu\text{m}$ , respectively (the 2 mmol case, that is the MFs). On the other hand, when choosing ethanol as the solvent of the solvothermal reaction, it can be inferred from Figure S4 in the Supporting Information that as the addition of  $\text{AuCl}_3$  was further increased to 20 mmol, the amount of as-generated gold particles exploded significantly that the  $\text{AgAuS}$  MSs were almost buried in them. It can be perceived from these changes that the added amount of  $\text{AuCl}_3$  did have a prominent impact on the final morphology of the Au–Ag–S composites. However, in consideration that the well-defined and uniform morphologies of these Au–Ag–S microstructures were fundamental to understanding the variation of SERS and photocatalytic performances on different substrates, only the  $\text{Ag}_2\text{S}$ –Au MF as well as Au– $\text{AgAuS}$  MS substrates were discussed in this work.

The SERS performance of the obtained  $\text{Ag}_2\text{S}$ –Au MF and Au– $\text{AgAuS}$  MS substrates toward the dilute solutions of DEHP and DEHA is shown in Figure 3. And the chemical structures and correspondingly recorded Raman spectra of as-purchased DEHP and DEHA liquids are exhibited in Figure S5–S6 in the Supporting Information. As can be observed clearly, the  $\text{Ag}_2\text{S}$ –Au MFs achieved  $1 \times 10^{-9}$  and  $1 \times 10^{-7}$  M of the LODs for DEHP and DEHA, whereas the Au– $\text{AgAuS}$  MSs achieved  $1 \times 10^{-7}$  and  $1 \times 10^{-6}$  M at the same time. In the case of the DEHP molecules (Figure 3c, d), the characteristic Raman bands located at 1168, 1275, 1430, and 1618  $\text{cm}^{-1}$  could be assigned to the C-ethyl asymmetric stretching mode, the C–C–C bending vibration and C–H in-plane bending vibration of the alkyl group, and the ring–ring stretching vibration of the *ortho*-phenyl group, respectively.<sup>6,38,39</sup> Meanwhile, for DEHA molecules (Figure 3a, b), the characteristic bands near 1344, 1450, and 1510  $\text{cm}^{-1}$  could be ascribed to the C–H in-plane bending vibration mode of the alkyl group and the bands at 1270 and 1302  $\text{cm}^{-1}$  could be attributed to the C–C–C bending vibration of the alkyl group while the bands near 1145 and 1394  $\text{cm}^{-1}$  should be assigned to the C-ethyl asymmetric stretching mode and the mixed mode of C–H in-plane bending vibration and C–C stretching mode of the alkyl group.<sup>6,38,39</sup> The differences between Raman spectra of Figure S6 in the Supporting Information and SERS spectra of Figure 3 could be due to many reasons. As discussed in the Introduction, it is attributed to both the chemical (i.e., CTR) and electromagnetic (i.e., LSPR) interactions between substrate surfaces and investigated compounds, which do not exist in pristine Raman spectra that SERS signals were obtained. Therefore, often the SERS spectra recorded on substrates show significant differences from Raman spectra, regarded as a known phenomenon. And herein, the SERS spectra of DEHP in Figure 3c, d basically matched well with previous literature

reports.<sup>6,40</sup> On the other hand, it is obvious that the  $\text{Ag}_2\text{S}$ –Au MFs achieved larger enhancement and hence lower LODs than Au– $\text{AgAuS}$  MSs. Because metallic structures (i.e., Au), as mentioned previously, usually play a dominant role in metal–semiconductor composites for enhancing Raman signals, it is rational that the SERS performance on substrates was closely related to the Au contents and morphologies of the composites. Therefore, the huge enhancement derived from the  $\text{Ag}_2\text{S}$ –Au MF substrates might be a result of mainly two aspects. First, SEM images have revealed the relatively higher Au content of the  $\text{Ag}_2\text{S}$ –Au MFs than Au– $\text{AgAuS}$  MSs which subsequently brought about better SERS performance. Second, the ternary  $\text{AgAuS}$  sheets, because of their ultrathin appearances, might have larger surface areas than  $\text{Ag}_2\text{S}$  particles, which would promote the SERS performance. Nevertheless, considering that the  $\text{Ag}_2\text{S}$ –Au MFs finally demonstrated better SERS performance than Au– $\text{AgAuS}$  MSs, the hierarchically assembled Au flowers in  $\text{Ag}_2\text{S}$ –Au MFs which have provided large numbers of closely spaced junctions of metallic surfaces, dubbed as the “hot spots” in the SERS process,<sup>41,42</sup> should have a greater impact.

Furthermore, the ethanol solutions of DEHP and DEHA were mixed with as-purchased orange juice in order to simulate the practical scenario of daily life and the recorded SERS spectra were displayed in Figure 4. The SERS spectrum of pure

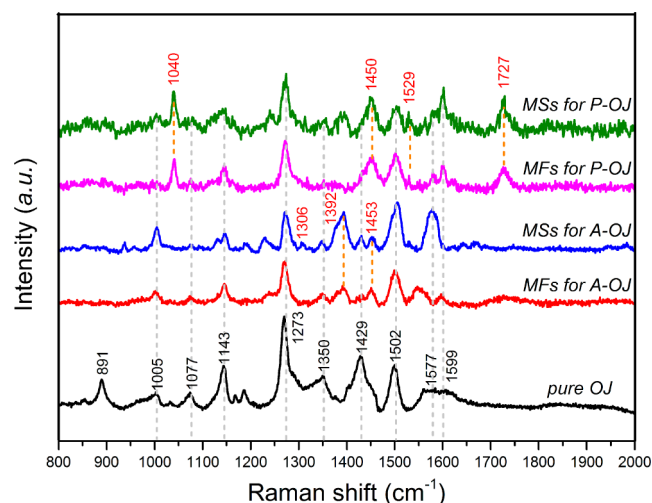


**Figure 4.** SERS spectra of as-purchased pure orange juice (OJ) as well as the mixtures of DEHA/ethanol solutions and OJ (A-OJ,  $0.9 \times 10^{-7}$  M for  $\text{Ag}_2\text{S}$ –Au MFs and  $0.9 \times 10^{-6}$  M for Au– $\text{AgAuS}$  MSs), DEHP/ethanol solutions and OJ (P-OJ,  $0.9 \times 10^{-9}$  M for  $\text{Ag}_2\text{S}$ –Au MFs and  $0.9 \times 10^{-7}$  M for Au– $\text{AgAuS}$  MSs).

orange juice shows fingerprint features of vitamin C and  $\beta$ -carotene and the specific band assignments are shown in Table S1 in the Supporting Information. It is discernible that the characteristic Raman bands at about 1040, 1450, 1529, and 1727  $\text{cm}^{-1}$  for DEHP, and 1306, 1392, as well as 1453  $\text{cm}^{-1}$  for DEHA, survived from interference of the bands of orange juice. The slight deviations of the Raman bands of DEHP and DEHA from those shown in Figure 3 might be caused by the variation of pH value after adding the acidic orange juice. Therefore, it can be concluded that the  $\text{Ag}_2\text{S}$ –Au MF substrates finally demonstrated the LODs of  $0.9 \times 10^{-9}$  M for DEHP and  $0.9 \times 10^{-7}$  M for DEHA in the mixtures while the Au– $\text{AgAuS}$  MS substrates achieved LODs of  $0.9 \times 10^{-7}$  M for DEHP and  $0.9 \times 10^{-6}$  M for DEHA as well. However, it is difficult for us to

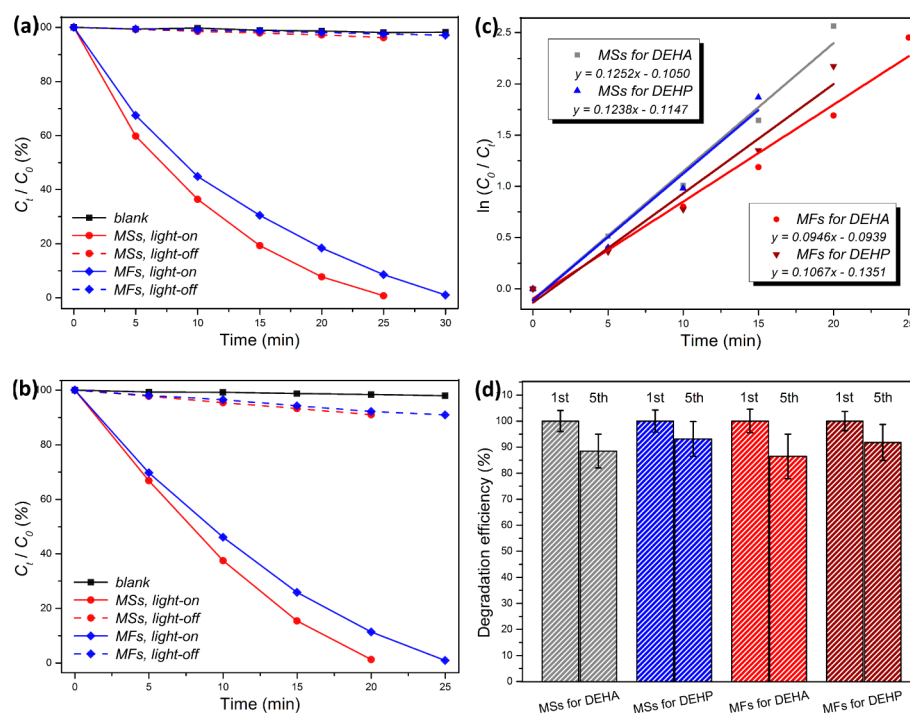


**Figure 5.** Time-dependent degradation efficiency of (a) DEHA and (b) DEHP ( $1 \times 10^{-5}$  M) under different conditions; (c) pseudo-first-order kinetic rate plots and correspondingly fitted kinetics equations of DEHA and DEHP degradation in the presence of different substrates; (d) recycling performance of different substrates presented in this work. (a–c)  $C_0$  and  $C_t$  represent the concentration of DEHA/DEHP at the time of 0 and  $t$  and were calculated, respectively, using the absorbance values at 213 nm for DEHA and 276 nm for DEHP, which were marked by (\*) in Figure S7 in the Supporting Information.

achieve the simultaneous detection of both DEHA and DEHP. Figure S5 in the Supporting Information has demonstrated that DEHA and DEHP possess similar chemical structures except the *ortho*-phenyl group of DEHP. Therefore, it is reasonable for DEHP and DEHA to show similar SERS spectra except those characteristic bands of *ortho*-phenyl-related modes, and in this case we can only know the existence or not of DEHP via the identification of *ortho*-phenyl-related bands, whereas we can not achieve simultaneous detection of DEHA and DEHP. But despite this fact, it should be possible for us to detect the plasticizer DEHA or DEHP along with another type of dye molecules such as rhodamine 6G and crystal violet, and thus achieve dual analyte detection on our substrates.

Figure 5 shows the photocatalytic performance of  $\text{Ag}_2\text{S}$ -Au MFs as well as Au-AgAuS MSs for degrading DEHA and DEHP under UV light irradiation, and the irradiation time-dependent UV-vis absorbance spectra of DEHA and DEHP ethanol solutions in the presence of Au-AgAuS MS substrate are also given in Figure S7 in the Supporting Information. As can be seen in panels a and b in Figure 5, it took the Au-AgAuS MSs 20 and 25 min to achieve complete degradation of DEHP and DEHA, whereas in the case of  $\text{Ag}_2\text{S}$ -Au MF substrate, it spent 25 and 30 min, respectively. The UV-vis-NIR diffuse reflectance spectra and correspondingly calculated band gap data of the substrates are shown in Figure S8 in the Supporting Information. As a result, the Au-AgAuS MSs possessed the band gap of 0.854 eV, which was a little larger than 0.832 eV of the  $\text{Ag}_2\text{S}$ -Au MFs. The previous XRD characterization has revealed that the AgAuS in Au-AgAuS MSs showed cubic  $Pm\bar{3}m$  structure (PDF#26-0728) with lattice constants of  $a = b = c = 5.010$  Å, whereas the  $\text{Ag}_2\text{S}$  in  $\text{Ag}_2\text{S}$ -Au MFs showed monoclinic  $P2_1/c$  structure with lattice constants of  $a = 4.229$  Å,  $b = 6.931$  Å, and  $c = 7.862$  Å. It is easy

to know that AgAuS possessed smaller lattice constants than  $\text{Ag}_2\text{S}$ . Hence in this regard, it is rational for AgAuS to have a larger band gap.<sup>43</sup> Figure 5c summarizes the kinetics equations ( $\ln(C_0/C_t) = kt + A$ ) of different substrates for degradation of DEHP/DEHA. The rate constants ( $k$ ) of Au-AgAuS MSs for degrading DEHP and DEHA were 0.1238 and 0.1252  $\text{min}^{-1}$  respectively while those of  $\text{Ag}_2\text{S}$ -Au MFs were 0.1067 and 0.0946  $\text{min}^{-1}$ . Compared with those single-component  $\text{Ag}_2\text{S}$  catalysts,<sup>20,44</sup> it can be inferred that the combination of  $\text{Ag}_2\text{S}$ / $\text{AgAuS}$  with Au has led to enhanced photocatalytic activities according to following mechanisms. Take the Au- $\text{Ag}_2\text{S}$  system as an example. First, as shown in Figure S9 in the Supporting Information, the energy level alignment in Au- $\text{Ag}_2\text{S}$  composites would be favorable for electron transfer from Au to the valence band of  $\text{Ag}_2\text{S}$ . Because the electrons donated by Au instinctively had higher energies, it should be easier for them to be excited to the conduction band of  $\text{Ag}_2\text{S}$  as photoelectrons and then served as reducing agents for degrading organic molecules. Besides, the metallic units (i.e., Au) may also enhance the photocatalytic efficiency by promoting charge separation at the metal-semiconductor (i.e., Au- $\text{Ag}_2\text{S}$ ) interfaces. The Au particles, because of their better electron affinity than  $\text{Ag}_2\text{S}$ , could serve as an electron sink to reserve the photogenerated electrons from  $\text{Ag}_2\text{S}$ , and hence inhibited the charge recombination, and finally promoted the photocatalytic efficiency.<sup>45,46</sup> On the other hand, the superior photocatalytic reactivity of the MSs than MFs here might be attributed to three factors. First, it can be observed from the previous SEM images that the AgAuS was the major component in Au-AgAuS MSs, whereas the  $\text{Ag}_2\text{S}$  was the minor component in  $\text{Ag}_2\text{S}$ -Au MFs. Considering the ability of semiconducting AgAuS/ $\text{Ag}_2\text{S}$  to generate photoelectrons and photoholes, the Au-AgAuS MSs should have the potential to

provide more photoelectrons/photoholes. Second, because  $\text{Ag}_2\text{S}$ –Au MFs possessed a smaller band gap than Au– $\text{AgAuS}$  MSs, it was easier for electron/hole recombination to occur on these occasions and thereby had adverse effects on their photocatalytic performance. Third, the ultrathin sheetlike shapes of  $\text{AgAuS}$  might have the potentiality to help the delocalization of the charge carriers along the normal and horizontal directions, thus delaying the electron/hole recombination process and promoting the degradation efficiency.<sup>47</sup> Figure 5d, in which the Au– $\text{AgAuS}$  MSs maintained about 88.5 and 93.1% of the efficiency for degrading DEHA and DEHP after experiencing five cycles of degradation reaction and the  $\text{Ag}_2\text{S}$ –Au MFs maintained about 86.4 and 91.8% of degradation efficiency as well, finally revealed the recyclability of the Au–Ag–S composite microstructures for photocatalytic plasticizer degradation, and thus further demonstrated the practical possibility they hold for novel efficient photocatalysts.

Finally, from a combinatorial point of view on the balance of SERS and photocatalytic activities and well-defined morphologies, it can be supposed that these Au–Ag–S composites have experienced two main periods in regard to the SERS and photocatalytic performance as the content of Au gradually increased. At first, as Au entered into the composite systems from nonexistence, the SERS and photocatalytic performance of the composites got enhanced simultaneously. On the one hand, analytes were bound to the generated Au surfaces, interacted with the LSPR of Au under laser excitation, and output stronger SERS signals than the case of pristine  $\text{Ag}_2\text{S}$ /AgAuS. On the other hand, the generated Au– $\text{Ag}_2\text{S}$ /AgAuS interfaces could also promote the photocatalytic efficiencies via both the charge transfer and charge separation mechanism. Therefore, it can be deduced that the SERS performance and photocatalytic activities got enhanced synergistically in this period. Afterward, if the Au content continued to increase, SERS performance may get further improved as more surfaces and junctions of Au were generated in spite of the loss of well-defined morphologies, nevertheless the photocatalytic activities may get depressed meanwhile as the surfaces which  $\text{Ag}_2\text{S}$ /AgAuS could provide to interact with plasticizer molecules were significantly reduced, as shown in Figure S4 in the Supporting Information. Therefore, it was regarded as an optimized ratio of the content of Au and  $\text{Ag}_2\text{S}$ /AgAuS for the MFs and MSs described in this work.

## CONCLUSIONS

In conclusion, for the first time, we have developed a facile single-step, one-pot solvothermal process for tailoring the Au–Ag–S composite microstructures for both SERS detection and photocatalytic degradation of the plasticizers DEHA and DEHP. Typically, well-defined  $\text{Ag}_2\text{S}$  particles inlaid Au microflowers ( $\text{Ag}_2\text{S}$ –Au MFs) as well as Au particles decorated  $\text{AgAuS}$  microsheets (Au– $\text{AgAuS}$  MSs) were successfully obtained. Amazingly, the  $\text{Ag}_2\text{S}$ –Au MF substrates demonstrated the LODs of as low as  $0.9 \times 10^{-9}$  and  $0.9 \times 10^{-7}$  M for DEHP and DEHA solutions in orange juice when exploited in SERS detection. Also, the Au– $\text{AgAuS}$  MS substrates achieved the LODs of  $0.9 \times 10^{-7}$  and  $0.9 \times 10^{-6}$  M for DEHP and DEHA in orange juice as well. Meanwhile, the Au– $\text{AgAuS}$  MSs demonstrated the ability to fully degrade the DEHP and DEHA molecules ( $1 \times 10^{-5}$  M) in ethanol solutions after 20 and 25 min of UV light irradiation which was rather efficient and recyclable. Also, in the case of the  $\text{Ag}_2\text{S}$ –Au MFs, it took 25 and 30 min for them to reach this goal. Considering not only

the facile preparation and intriguing morphologies but also their inspiring SERS and photocatalytic activities toward common plasticizers, it is believable that these dual-active Au–Ag–S composite microstructures hold great potential for various environment-related applications like novel multifunctional sensing and monitoring chips or devices.

## ASSOCIATED CONTENT

### Supporting Information

The experimental details, Figure S1–S9, and Table S1 are included. This material is available free of charge via the Internet at <http://pubs.acs.org>.

## AUTHOR INFORMATION

### Corresponding Author

\*E-mail: [rcche2008@gmail.com](mailto:rcche2008@gmail.com).

### Notes

The authors declare no competing financial interest.

## ACKNOWLEDGMENTS

This work was financially supported by the National Natural Foundation of China (11274066, 51172047, 50872145, and 51102050) and the Ministry of Science and Technology of China (973 Projects 2013CB932901 and 2009CB930803). In addition, the authors are grateful to the “Shu Guang” project supported by Shanghai Municipal Education Commission and Shanghai Education Development Foundation (09SG01).

## REFERENCES

- (1) Gray, L. E.; Ostby, J.; Furr, J.; Price, M.; Veeramachaneni, D. N. R.; Parks, L. Perinatal Exposure to the Phthalates DEHP, BBP, and DINP, but Not DEP, DMP, or DOTP, Alters Sexual Differentiation of the Male Rat. *Toxicol. Sci.* **2000**, *58*, 350–365.
- (2) Ghisari, M.; Bonefeld-Jorgensen, E. C. Effects of Plasticizers and Their Mixtures on Estrogen Receptor and Thyroid Hormone Functions. *Toxicol. Lett.* **2009**, *189*, 67–77.
- (3) Wang, S.; Xu, Z. X.; Fang, G. Z.; Duan, Z. J.; Zhang, Y.; Chen, S. Synthesis and Characterization of a Molecularly Imprinted Silica Gel Sorbent for the On-Line Determination of Trace Sudan I in Chilli Powder through High-Performance Liquid Chromatography. *J. Agric. Food Chem.* **2007**, *55*, 3869–3876.
- (4) Huang, G. M.; Zheng, O. Y.; Cooks, R. G. High-Throughput Trace Melamine Analysis in Complex Mixtures. *Chem. Commun.* **2009**, 556–558.
- (5) Ai, K. L.; Liu, Y. L.; Lu, L. H. Hydrogen-Bonding Recognition-Induced Color Change of Gold Nanoparticles for Visual Detection of Melamine in Raw Milk and Infant Formula. *J. Am. Chem. Soc.* **2009**, *131*, 9496–9497.
- (6) Peng, B.; Li, G. Y.; Li, D. H.; Dodson, S.; Zhang, Q.; Zhang, J.; Lee, Y. H.; Demir, H. V.; Ling, X. Y.; Xiong, Q. H. Vertically Aligned Gold Nanorod Monolayer on Arbitrary Substrates: Self-Assembly and Femtomolar Detection of Food Contaminants. *ACS Nano* **2013**, *7*, 5993–6000.
- (7) Shao, M. W.; Lu, L.; Wang, H.; Wang, S.; Zhang, M. L.; Ma, D. D.; Lee, S. T. An Ultrasensitive Method: Surface-Enhanced Raman Scattering of Ag Nanoparticles from  $\beta$ -Silver Vanadate and Copper. *Chem. Commun.* **2008**, 2310–2312.
- (8) Bell, S. E. J.; Sirimuthu, N. M. S. Rapid, Quantitative Analysis of ppm/ppb Nicotine Using Surface-Enhanced Raman Scattering from Polymer-Encapsulated Ag Nanoparticles (Gel-Colls). *Analyst* **2004**, *129*, 1032–1036.
- (9) Contreras-Caceres, R.; Abade-Cela, S.; Guardia-Giros, P.; Fernandez-Barbero, A.; Perez-Juste, J.; Alvarez-Puebla, R. A.; Liz-Marzan, L. M. Multifunctional Microgel Magnetic/Optical Traps for SERS Ultradetection. *Langmuir* **2011**, *27*, 4520–4525.



- (10) Cecchini, M. P.; Turek, V. A.; Paget, J.; Kornyshev, A. A.; Edell, J. B. Self-Assembled Nanoparticle Arrays for Multiphase Trace Analyte Detection. *Nat. Mater.* **2013**, *12*, 165–171.
- (11) Ma, W.; Kuang, H.; Xu, L. G.; Ding, L.; Xu, C. L.; Wang, L. B.; Kotov, N. A. Attomolar DNA Detection with Chiral Nanorod Assemblies. *Nat. Commun.* **2013**, *4*, 2689.
- (12) Nie, S. M.; Emery, S. R. Probing Single Molecules and Single Nanoparticles by Surface-Enhanced Raman Scattering. *Science* **1997**, *275*, 1102–1106.
- (13) Liu, H. W.; Zhang, L.; Lang, X. Y.; Yamaguchi, Y.; Iwasaki, H.; Inouye, Y.; Xue, Q. K.; Chen, M. W. Single Molecule Detection from A Large-Scale SERS-Active Au<sub>70</sub>Ag<sub>21</sub> Substrate. *Sci. Rep.* **2011**, *1*, 112.
- (14) Yang, X. L.; Zhong, H.; Zhu, Y. H.; Shen, J. H.; Li, C. Z. Ultrasensitive and Recyclable SERS Substrate Based on Au-Decorated Si Nanowire Arrays. *Dalton Trans.* **2013**, *42*, 14324–14330.
- (15) Li, X. L.; Hu, H. L.; Li, D. H.; Shen, Z. X.; Xiong, Q. H.; Li, S. Z.; Fan, H. J. Ordered Array of Gold Semishells on TiO<sub>2</sub> Spheres: An Ultrasensitive and Recyclable SERS Substrate. *ACS Appl. Mater. Interfaces* **2012**, *4*, 2180–2185.
- (16) Chen, Y. J.; Tian, G. H.; Pan, K.; Tian, C. G.; Zhou, J.; Zhou, W.; Ren, Z. Y.; Fu, H. G. *In Situ* Controlled Growth of Well-Dispersed Gold Nanoparticles in TiO<sub>2</sub> Nanotube Arrays as Recyclable Substrates for Surface-Enhanced Raman Scattering. *Dalton Trans.* **2012**, *41*, 1020–1026.
- (17) Zou, X. X.; Silva, R.; Huang, X. X.; Al-Sharab, J. F.; Asefa, T. A Self-Cleaning Porous TiO<sub>2</sub>-Ag Core-Shell Nanocomposite Material for Surface-Enhanced Raman Scattering. *Chem. Commun.* **2013**, *49*, 382–384.
- (18) Zhou, Y.; Chen, J.; Zhang, L.; Yang, L. B. Multifunctional TiO<sub>2</sub>-Coated Ag Nanowire Arrays as Recyclable SERS Substrates for the Detection of Organic Pollutants. *Eur. J. Inorg. Chem.* **2012**, 3176–3182.
- (19) Lin, Y.; Bunker, C. E.; Fernando, K. A. S.; Connell, J. W. Aqueously Dispersed Silver Nanoparticle-Decorated Boron Nitride Nanosheets for Reusable, Thermal Oxidation-Resistant Surface Enhanced Raman Spectroscopy (SERS) Devices. *ACS Appl. Mater. Interfaces* **2012**, *4*, 1110–1117.
- (20) Cao, Q.; Che, R. C.; Chen, N. Facile and Rapid Growth of Ag<sub>2</sub>S Microrod Arrays as Efficient Substrates for Both SERS Detection and Photocatalytic Degradation of Organic Dyes. *Chem. Commun.* **2014**, *50*, 4931–4933.
- (21) Xu, B. B.; Zhang, Y. L.; Wei, S.; Ding, H.; Sun, H. B. On-Chip Catalytic Microreactors for Modern Catalysis Research. *ChemCatChem* **2013**, *5*, 2091–2099.
- (22) Xu, B. B.; Zhang, R.; Liu, X. Q.; Wang, H.; Zhang, Y. L.; Jiang, H. B.; Wang, L.; Ma, Z. C.; Ku, J. F.; Xiao, F. H.; Sun, H. B. On-Chip Fabrication of Silver Microflow Array as a Catalytic Microreactor for Allowing *in situ* SERS Monitoring. *Chem. Commun.* **2012**, *48*, 1680–1682.
- (23) Salmistraro, M.; Schwartzberg, A.; Bao, W.; Depero, L. E.; Weber-Bargioni, A.; Cabrini, S.; Alessandri, I. Triggering and Monitoring Plasmon-Enhanced Reactions by Optical Nanoantennas Coupled to Photocatalytic Beads. *Small* **2013**, *9*, 3301–3307.
- (24) Muniz-Miranda, M. SERS Monitoring of the Catalytic Reduction of 4-nitrophenol on Ag-Doped Titania Nanoparticles. *Appl. Catal., B* **2014**, *146*, 147–150.
- (25) Wen, C. Y.; Liao, F.; Liu, S. S.; Zhao, Y.; Kang, Z. H.; Zhang, X. L.; Shao, M. W. Bi-functional ZnO-RGO-Au Substrate: Photocatalysts for Degrading Pollutants and SERS Substrates for Real-Time Monitoring. *Chem. Commun.* **2013**, *49*, 3049–3051.
- (26) Li, R. Z.; Zhou, A. H.; Lu, Q.; Yang, C. Z.; Zhang, J. D. *In Situ* Monitoring and Analysis of the Photocatalytic Degradation Process and Mechanism on Recyclable Au NPs-TiO<sub>2</sub> NTs Substrate Using Surface-Enhanced Raman Scattering. *Colloids Surf., A* **2013**, *436*, 270–278.
- (27) Islam, S. K.; Tamargo, M.; Moug, R.; Lombardi, J. R. Surface-Enhanced Raman Scattering on a Chemically Etched ZnSe Surface. *J. Phys. Chem. C* **2013**, *117*, 23372–23377.
- (28) Lombardi, J. R.; Birke, R. L. A Unified Approach to Surface-Enhanced Raman Spectroscopy. *J. Phys. Chem. C* **2008**, *112*, 5605–5617.
- (29) Bao, Z. H.; Sun, Z. H.; Xiao, M. D.; Tian, L. W.; Wang, J. F. Hydrothermal Transformation from Au Core-Sulfide Shell to Au Nanoparticle-Decorated Sulfide Hybrid Nanostructures. *Nanoscale* **2010**, *2*, 1650–1652.
- (30) Zhang, Y.; Zhang, Y. J.; Hong, G. S.; He, W.; Zhou, K.; Yang, K.; Li, F.; Chen, G. C.; Liu, Z.; Dai, H. J.; Wang, Q. B. Biodistribution, Pharmacokinetics and Toxicology of Ag<sub>2</sub>S Near-Infrared Quantum Dots in Mice. *Biomaterials* **2013**, *34*, 3639–3646.
- (31) Hocaoglu, I.; Cizmeciyan, M. N.; Erdem, R.; Ozen, C.; Kurt, A.; Sennaroglu, A.; Acar, H. Y. Development of Highly Luminescent and Cytocompatible Near-IR-Emitting Aqueous Ag<sub>2</sub>S Quantum Dots. *J. Mater. Chem.* **2012**, *22*, 14674–14681.
- (32) Huang, H. W.; Liu, X. Y.; Zeng, Y. L.; Yu, X. Y.; Liao, B.; Yi, P. G.; Chu, P. K. Optical and Biological Sensing Capabilities of Au<sub>2</sub>S/AuAgS Coated Gold Nanorods. *Biomaterials* **2009**, *30*, S622–S630.
- (33) Sun, Z. H.; Yang, Z.; Zhou, J. H.; Yeung, M. H.; Ni, W. H.; Wu, H. K.; Wang, J. F. A General Approach to the Synthesis of Gold-Metal Sulfide Core-Shell and Heterostructures. *Angew. Chem., Int. Ed.* **2009**, *48*, 2881–2885.
- (34) Huang, H. W.; Qu, C. T.; Liu, X. Y.; Huang, S. W.; Xu, Z. J.; Liao, B.; Zeng, Y. L.; Chu, P. K. Preparation of Controllable Core-Shell Gold Nanoparticles and Its Application in Detection of Silver Ions. *ACS Appl. Mater. Interfaces* **2011**, *3*, 183–190.
- (35) Zhu, Y. F.; Fan, D. H.; Shen, W. Z. Chemical Conversion Synthesis and Optical Properties of Metal Sulfide Hollow Microspheres. *Langmuir* **2008**, *24*, 11131–11136.
- (36) Nilsen, W. G. Raman Spectrum of Cubic ZnS. *Phys. Rev.* **1969**, *182*, 838–850.
- (37) Boya, R.; Jayaraj, D.; Kulkarni, G. U. Top-Contacting Molecular Monolayers Using Single Crystalline Au Microplate Electrodes. *Chem. Sci.* **2013**, *4*, 2530–2535.
- (38) Han, X. X.; Jia, H. Y.; Wang, Y. F.; Lu, Z. C.; Wang, C. X.; Xu, W. Q.; Zhao, B.; Ozaki, Y. Analytical Technique for Label-Free Multi-Protein Detection Based on Western Blot and Surface-Enhanced Raman Scattering. *Anal. Chem.* **2008**, *80*, 2799–2804.
- (39) Chen, Y.; Yi, Z.; Chen, S. J.; Luo, J. S.; Yi, Y. G.; Tang, Y. J. Study of Density Functional Theory for Surface-Enhanced Raman Spectra of *p*-Aminothiophenol. *Spectrosc. Spect. Anal.* **2011**, *31*, 2952–2955.
- (40) An, Q.; Zhang, P.; Li, J. M.; Ma, W. F.; Guo, J.; Hu, J.; Wang, C. C. Silver-Coated Magnetite-Carbon Core-Shell Microspheres as Substrate-Enhanced SERS Probes for Detection of Trace Persistent Organic Pollutants. *Nanoscale* **2012**, *4*, 5210–5216.
- (41) Cong, V. T.; Ganbold, E. O.; Saha, J. K.; Jang, J.; Min, J.; Choo, J.; Kim, S.; Song, N. W.; Son, S. J.; Lee, S. B.; Joo, S. W. Gold Nanoparticle Silica Nanopeapods. *J. Am. Chem. Soc.* **2014**, *136*, 3833–3841.
- (42) Mirsaleh-Kohan, N.; Iberi, V.; Simmons, P. D.; Bigelow, N. W.; Vaschillo, A.; Rowland, M. M.; Best, M. D.; Pennycook, S. J.; Masiello, D. J.; Guiton, B. S. Single-Molecule Surface-Enhanced Raman Scattering: Can STEM/EELS Image Electromagnetic Hot Spots? *J. Phys. Chem. Lett.* **2012**, *3*, 2303–2309.
- (43) Huang, L. Y.; Lambrecht, W. R. L. Electronic Band Structure, Phonons, and Exciton Binding Energies of Halide Perovskites CsSnCl<sub>3</sub>, CsSnBr<sub>3</sub>, and CsSnI<sub>3</sub>. *Phys. Rev. B* **2013**, *88*, 165203.
- (44) Neelgund, G. M.; Oki, A. Photocatalytic Activity of CdS and Ag<sub>2</sub>S Quantum Dots Deposited on Poly(amidoamine) Functionalized Carbon Nanotubes. *Appl. Catal., B* **2011**, *110*, 99–107.
- (45) Xu, L.; Yin, Z. Y.; Cao, S. W.; Fan, Z. X.; Zhang, H.; Xue, C. Rational Synthesis of Triangular Au-Ag<sub>2</sub>S Hybrid Nanoframes with Effective Photoresponses. *Chem. - Eur. J.* **2014**, *20*, 2742–2745.
- (46) Cao, S. W.; Yin, Z.; Barber, J.; Boey, F. Y. C.; Loo, S. C. J.; Xue, C. Preparation of Au-BiVO<sub>4</sub> Heterogeneous Nanostructures as Highly Efficient Visible-Light Photocatalysts. *ACS Appl. Mater. Interfaces* **2012**, *4*, 418–423.



(47) Xu, T. G.; Zhang, C.; Shao, X.; Wu, K.; Zhu, Y. F. Monomolecular-Layer  $\text{Ba}_5\text{Ta}_4\text{O}_{15}$  Nanosheets: Synthesis and Investigation of Photocatalytic Properties. *Adv. Funct. Mater.* **2006**, *16*, 1599–1607.